Multiple Hopf bifurcations and flow dynamics inside a 2D singular lid driven cavity

Lucas Lestandi, Swagata Bhaumik, G.R.K.C. Avatar, Mejdi Azaiez, Tapan Sengupta

Multiple Hopf bifurcations and flow dynamics inside a 2D singular lid driven cavity

Lucas Lestandi, Swagata Bhaumik*, G. R. K. C. Avatar*, Mejdi Azaiez, Tapan K. Sengupta*

I2M Laboratory, Univ. of Bordeaux, France
**HPCL, IIT Kanpur, Kanpur, India*

Abstract

Two-dimensional (2D) flow inside a lid driven cavity (LDC) is shown to display multi-modal behavior in a consistent manner following the first Hopf bifurcation with varying Reynolds numbers (Re), depending upon the chosen spatial and temporal discretization scheme. Direct numerical simulation (DNS) following impulsive start, is used to show spatio-temporal growth and its nonlinear saturation of disturbance growth. Despite the fact that researchers have produced different value of Reynolds number when first Hopf bifurcation occurs (Re_{cr1}), DNS fundamentally differs from classical bifurcation studies involving global instability study of an equilibrium flow due to adopted nonlinear approach and not restricting the analysis to temporal instability only. The accuracy attribute of the DNS adopted here has been shown conclusively earlier via demonstration of a weak transient polygonal core vortex surrounded by relatively stronger gyrating vortices, which appear as a constellation after the disappearance of the transient, in Sengupta *et al.* (J. Comput. Phys., **228**, 3048- 3071 and 6150-6168 (2009)). Investigated LDC flow is characterized by multiple time scales at any Re, which are weak function of Re in selective intervals, punctuated by multiple bifurcations. The present investigation achieves two primary goals. First, it proposes to reconcile that Re_{cr1} obtained by different numerical approaches can be shown to be in same range, provided the equilibrium flow obtained

Email addresses: llestandi@u-bordeaux.fr (Lucas Lestandi), swagata@iitk.ac.in (Swagata Bhaumik*), krishnachand.beaero14@pec.edu.in (G. R. K. C. Avatar*), azaiez@enscbp.fr (Mejdi Azaiez), tksen@iitk.ac.in (Tapan K. Sengupta*)

is of good quality, untainted by excessive diffusion. Secondly, we also show that for increasing Re following the first Hopf bifurcation, the flow during the limit cycle suffers a secondary instability, thus, requiring computation of the flow field over a longer time period. The first goal is met by exciting the flow field with a pulsating vortex inside the LDC for a very high accuracy scheme, we are able to show the universal nature of the primary bifurcation for Re in the range between 8020 and 8025. The flow at higher Re displays significantly increased spectral peaks, including broad-band spectrum and the understanding of all these have been aided by phase space portraits.

Keywords: Lid driven cavity, DNS, Multiple Hopf bifurcation, polygonal core vortex, phase space portrait

---

1. Introduction

The 2D flow in a square LDC (of side L) is a popular problem to test new algorithms for incompressible Navier-Stokes equation (NSE) due to its unambiguous boundary conditions, coupled with its very simple geometry. As the lid is given a constant-speed translation (U), this gives rise to corner singularities on the top wall, as depicted in the top frame of Fig. 1. The role of such singularities is to give rise to Gibbs' phenomenon, as reported by pseudo-spectral computation of NSE [2, 7]. Computing flow in LDC by other discrete computing methods [9, 17, 33], corner singularities do not cause any problem due to smoothly decaying spectrum created by spatial discretization [37] near the cutoff wavenumber. While it is possible to compute steady flow at low Re by various methods including lowest order spatial discretization, it is not so at higher Re, where the flow displays inherent tendencies of unsteadiness. One of the central activities in studying the problem of LDC is to show that the onset of unsteadiness is related to flow instability. Viewed in this perspective, the primary goal is then predict the correct equilibrium flow for global instability studies. However, in DNS one directly proceeds to obtain the unsteady flow. This latter approaches can thus cause confusion, as is noted in the published literature. Many low order methods are incapable of computing unsteady flows at high Re ($= UL/\nu$), where ν is the kinematic viscosity. In Ghia *et al.* [17], results for a wide range of Re up to 10000 are presented. The flow is steady for $Re = 10000$ in [17], while numerical results obtained by high accuracy combined compact difference (CCD) scheme presented in [26, 27] indicate creation of a transient polyg-

onal vortex at the core, with permanent gyrating satellite vortices around it. In these references, sixth order CCD scheme has been used to discretize both the convection and diffusion terms of the vorticity transport equation. It is well known [1, 36] that compact schemes for spatial discretization filters minimally, as compared to other methods.

For the LDC problem at $Re \leq 1000$, researchers [2, 3, 7] have tried to circumvent the singularity by subtracting the contribution due to singularity (divergence of pressure and vorticity at the top corners) to obtain a steady flow solution by pseudo-spectral methods. The singularity diverges as $1/r$, with r as the radial distance from the corner for the flow, by including inertial effects [20]. This method has not been used for Re exceeding 1000 and instead for higher Re, singularity is removed by altering the velocity boundary condition on the lid - a process known as the *regularization* [25].

A steady solution has been reported by many [6, 14, 17] for Re far exceeding the values reported in the literature for the first Hopf Bifurcation (Re_{cr1}), due to the excessive diffusion of the discretization. If this steady solution is treated as equilibrium solution, then its global instability will not be predicted in a unique manner, as have been attempted by solving numerically the bifurcation problem [6, 16, 30]. Use of lower order methods in obtaining equilibrium flow results in contaminated eigenvalues. On the other hand, simulations of full time-dependent NSE [18, 19, 28] reveal that the flow loses stability via a Hopf bifurcation with respect to increasing Re. Critical Re_{cr1} and frequencies obtained from DNS and eigenvalue analysis do not match and such differences are noted for different DNS results too for various reasons, some of these will be explained here.

It is shown in [27, 28, 38] that Re_{cr1} depends upon the accuracy of the method and how the flow is established in DNS. Physically, impulsively started flow is ideal to study the dynamics, as it triggers all frequencies at $t = 0$ [26, 27]. Such an analysis is preferred and is superior to normal mode analysis of eigenvalue approach. We note that obtaining a limit cycle at a different Re from the limit cycle solution obtained at another Re is not appropriate. While this may result in faster computations [28], this also produces different Re_{cr1}, as compared to the results obtained by impulsive start [26, 27, 38]. This is highlighted here by the high accuracy study of Hopf bifurcations by DNS performed by reducing sources of error.

Multiple Hopf bifurcations have been reported earlier by researchers for LDC flow. Authors in [3] have talked about a second bifurcation, while Sengupta et al. [38] have described multiple Hopf bifurcations for flow in

LDC by plotting the bifurcation diagram using FFT data of vorticity time series. In recent times, Girault et al. [46] have talked about multiple Hopf bifurcations for LDC flow using compact scheme. Thus, the present effort in reporting multiple Hopf bifurcation is based on relating it with overall dynamics of the flow field, as computed by the high accuracy method, which is being used for LDC flow in [26, 27, 38] and in the present study.

The role of various sources of errors, including aliasing error for flow inside LDC has been described in [27]. Here we will discuss the roles of other sources of errors, based on the model convection-diffusion error [41]. As this simulations are extremely sensitive to operating conditions, the present work relies only on sequential computing in order to capture the weak transient core vortex when the major sources of errors are removed. This aspect of hyper-sensitivity of computed solution on background disturbance is further exploited here to explain why Re_{cr1} are different for different numerical methods.

Appearance of unsteadiness with variation in parameter value(s) studied by bifurcation theory [39] is due to flow instabilities [35]. Linear instability of equilibrium flow and DNS have been used in the literature to evaluate the onset of unsteadiness, providing scattered values of Re_{cr1} for flow in LDC. The authors in [3], using a second order projection method along with second order backward difference for time integration, obtained this value to be bracketed between 8017.6 to 8018.8. The authors furthermore added that their preliminary analysis beyond the first bifurcation led them *to suppose that the system passes through a second Hopf bifurcation for a second critical Reynolds number located in the interval [9687, 9765).* Various researchers noted different value of Re_{cr1}: As 8031.93 in [32], 7972 in Cazemier *et al.* [11] using a finite volume method. Bruneau and Saad [8] noted this to be in the range of 8000 to 8050 without showing the relevant bifurcation diagram, using a third order upwind scheme, using (1024×1024) grid. However, the use of three time-level Gear method, produces a spurious mode to affect results. We highlight the roles played by different numerical sources in triggering flow unsteadiness by Re_{cr1}, that explains the scatter of reported Re_{cr1}. Of specific interest are for methods using very high accuracy methods which report relatively high values of Re_{cr1}. It is somewhat paradoxical that very diffusive upwind methods produce very high Re_{cr1} also, by attenuating disturbances to delay unsteadiness, as reported in [6, 14, 17].

High accuracy compact schemes have been used in Sengupta *et al.* [38] and described multiple Hopf bifurcations, showing $Re_{cr1} = 7933$ and the sec-

ond at 8187, using the FFT amplitude of the vorticity time series obtained using sixth order accurate combined compact difference (NCCD) scheme on a uniform (257×257) grid. Osada and Iwatsu [28] have identified this value at $7987 \pm 2\%$ - in similar range using compact scheme on non-uniform (128×128) and (257×257)-grids. This limit is obtained based on linear interpolation of data from these two grids, in Fig. 3 of [28] for u-component of velocity at the core of LDC. The figure clearly shows grid dependence of the computed results as the A_e^2 versus Re curves have diverging slopes. Thus, the authors obtained grid-dependent results, as seen in the present computations. This is due to the fact that the wall vorticity is different for different wall resolution, and here we explain the reason for this. Here all computations are obtained by starting from quiescent condition at $t = 0$, following an impulsive start. Several results in [28] are obtained by projecting results from one Re to another. Here, we will demonstrate that projecting a solution from one Re to another is essentially flawed to obtain Re_{cr1}. In [28], the authors also provide the second critical Reynolds number as $Re_{cr2} = 9575 \pm 3\%$, which is quite different from that is given in [3].

There are also studies which report widely different values of Re_{cr1}. For example, Shen [34] reported Re_{cr1} in the range of 10000 to 10500. Poliashenko and Aidun [30] on the other hand reported a value of $Re_{cr1} = 7763 \pm 2\%$ using a commercial FEM package. Peng *et al.* [29] reported a value of $Re_{cr1} = 7402 \pm 4\%$ using FDM by Marker and Cell (MAC) method.

To obtain Re_{cr1}, DNS is preferred over eigenvalue analysis, as in the latter a temporal analysis assumes all points to have identical time variation. In DNS, the true spatio-temporal dynamics is traced. In the schematic shown on top of Fig. 1, five points are identified where time variation of vorticity is stored, as shown in the other frames of the figure. Apart from the center of the LDC, there are two points at the bottom embedded inside corner vortices at $(x = 0.02, y = 0.02)$ and $(x = 0.98, y = 0.02)$. Other two points located near the top right corner of the cavity at $(x = 0.95, y = 0.95)$ and $(x = 0.99, y = 0.99)$, display higher unsteadiness, strongly affected by aliasing error [27]. This is noted in the vorticity time series shown in Fig. 1. The core suffers least perturbation and the next higher disturbance amplitude is noted at the bottom right corner. While bottom left corner point registers significant vorticity disturbance, the top right corner points log higher disturbance vorticity. The point at $(x = 0.99, y = 0.99)$ being closest to the corner singularity, displays highest variations and takes longer to attain the limit cycle. Hence the point $(x = 0.95, y = 0.95)$ is preferred for analysis

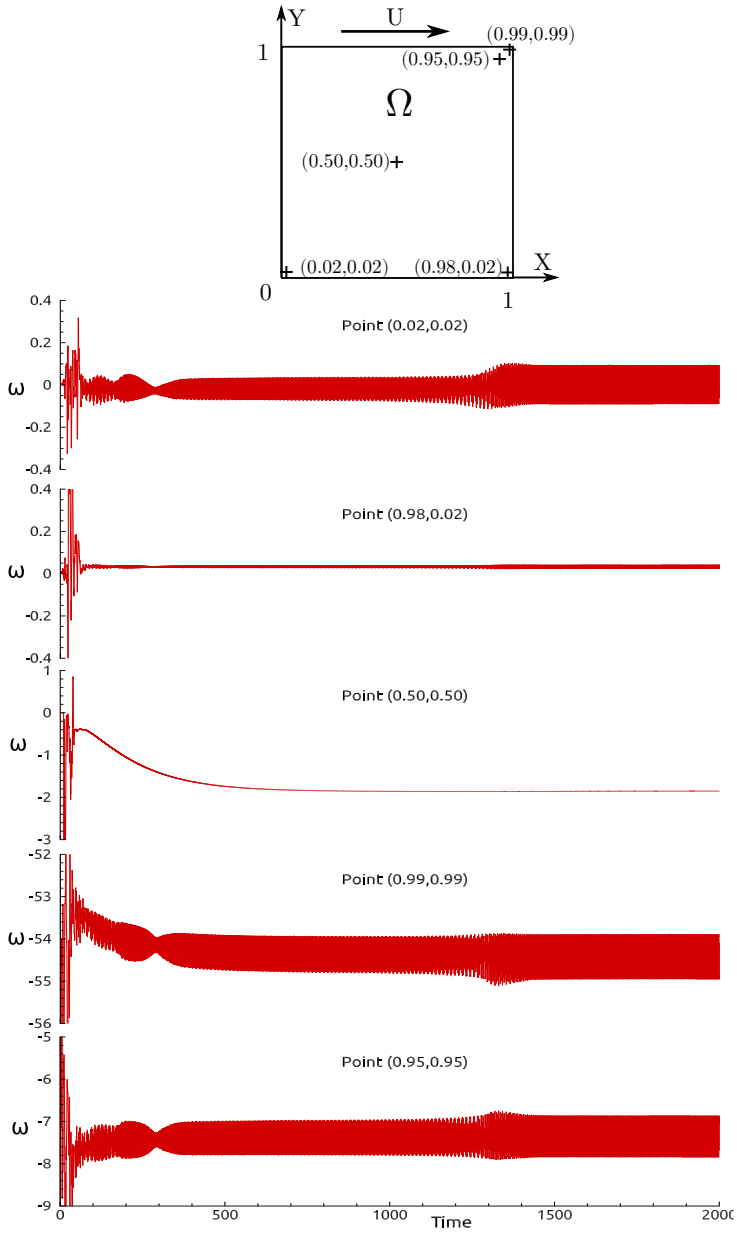

Figure 1: The schematic of the computational domain and location of sampling points (top) and vorticity time series at the sampling points obtained for $Re = 9500$ obtained from solution of Navier-Stokes equation using a (257×257) grid.

purpose [26, 27, 38]. In [28], the time series has been sampled at a point near the bottom right corner at $(x = 13/16, y = 1/16)$.

The paper is formatted in the following manner. In the next section, a very brief recap of the governing equation and the numerical methods used are provided. In section 3, the flow field is characterized by vorticity field obtained by DNS with Re. Vorticity dynamics and polygonal core vortex are described in section 4. This is followed by description of multiple Hopf bifurcations in section 5. Apart from describing new equilibrium states, we also show the frequency spectrum of the flow field as a function of Re and provide the phase space trajectory to describe the flow dynamics. In the following section 6, we discuss about extreme sensitivity to the grid resolution and projection of solution for one parameter to another. Most importantly we explain receptivity of the flow to imposed excitation and trace back the universal Re_{cr1}, which we consider as the main results in the present work. In the end, summary and conclusions are provided.

2. Governing Equations and Numerical Methods

DNS of the 2D flow is carried out by solving NSE in stream function-vorticity formulation given by,

$$\nabla^2\psi = -\omega \tag{1}$$

$$\frac{\partial\omega}{\partial t} + (\vec{V}\cdot\nabla)\omega = \frac{1}{Re}\nabla^2\omega \tag{2}$$

where ω is the non-zero out-of-plane component of vorticity for the 2D problem. The velocity is related to the stream function by $\vec{V} = \nabla \times \vec{\Psi}$, where $\vec{\Psi} = [0\ 0\ \psi]$. Reynolds number is defined by L and the constant lid velocity, (U), which are also used as length and velocity scales for non-dimensionalization. This formulation is preferred due to inherent solenoidality of the velocity and vorticity for 2D flows. It also allows one to circumvent the pressure-velocity coupling problem. The numerical methods and the dynamics of the flow for $Re = 10000$ are given in greater details elsewhere [26, 27] and is not repeated here.

Equations (1) and (2) are solved subject to the following boundary conditions. On all the four walls of LDC, $\psi = constant$ is prescribed which helps in satisfying no-slip condition; the wall vorticity is $\omega_b = -\frac{\partial^2 \psi}{\partial n^2}$, with n as the wall-normal co-ordinate chosen for the four segments of the cavity to obtain the boundary vorticity. This is calculated using Taylors series expansion at all the walls with appropriate velocity conditions at the boundary segments. The top lid moves horizontally with a unit nondimensional velocity, with all other walls as stationary. To solve the discretized form of Eq. (1), Bi-CGSTAB method has been used here, which is a fast and convergent elliptic PDE solver [42]. The convection and diffusion terms are discretized using the NCCD method [26, 27], which obtains both first and second derivatives simultaneously. All other details about NCCD and other compact schemes can be also found in Sengupta [36] and hence are not reproduced here. For time advancing Eq. (2), four-stage, fourth-order Runge-Kutta (RK4) method is used that is tuned to preserve dispersion relation. The NCCD scheme has been analyzed for resolution and effectiveness in discretizing the diffusion terms along with the dispersion relation preservation properties for 1D convection equation [26, 27]. It is noted that the NCCD method is efficient, providing high resolution and effective diffusion discretization. Additionally, the method has built-in ability to control aliasing error. The only drawback of NCCD scheme is that it can be used only with uniform structured grids. All computations are performed with non-dimensional time-step of $dt = 0.001$. The final limit cycle behaves in a similar fashion, when time step is changed. Only the instability of the limit cycle appears at different time range with change in dt. We also report an additional set of computations using a finer grid with (513×513) points. Vorticity time series at a sampling point, qualitatively remains the same, with only the mean value shifted by a small fraction. The sampling point location being at (0.95,0.95) has been explained in the previous section with respect to sampling point taken in [28].

3. Dynamics of singular LDC Flow

To understand why the eigenvalue analysis and direct solution of NSE do not match, we explain this further with the help of Fig. 2 for $Re = 8800$, which shows the vorticity time series at ($x = 0.95$, $y = 0.95$) in the central frame. The results are obtained by solving unsteady NSE using NCCD scheme [26, 27, 38] for spatial discretizations of first and second derivatives.

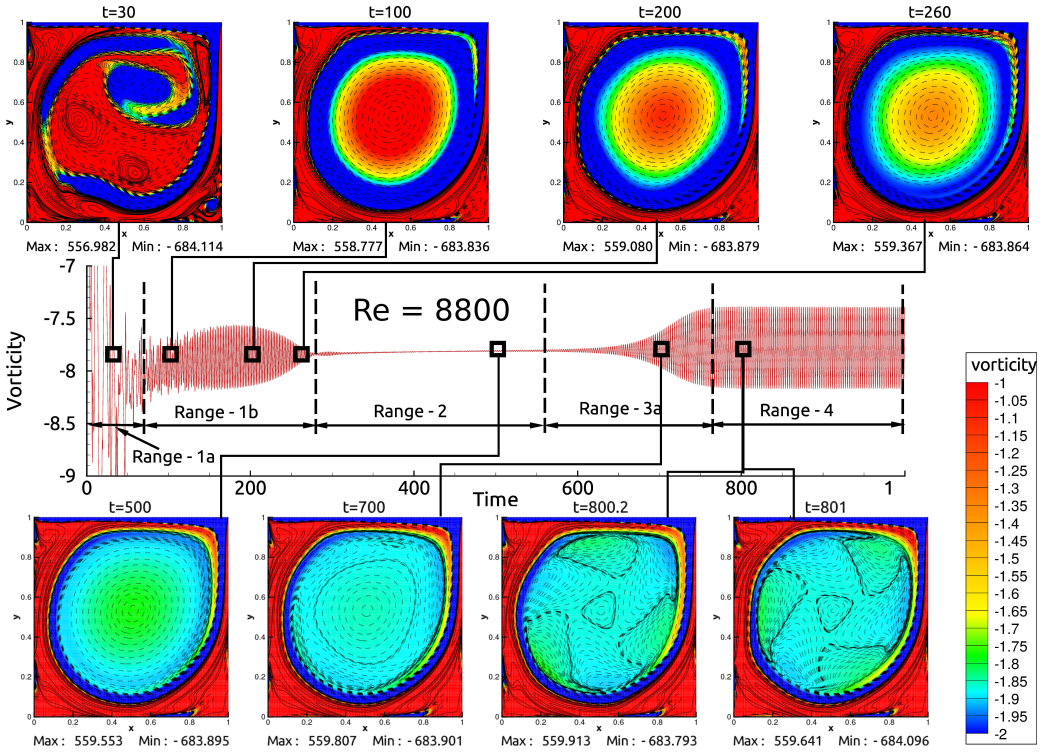

Figure 2: The vorticity time series at the sampling point ($x = 0.95, y = 0.95$) obtained for $Re = 8800$ with vorticity contour plots shown at the indicated time instants. Solution of Navier-Stokes equation is obtained using (257×257) grid.

In the time series, we have identified various regimes of time-variation. For example, in Range-1a of Fig. 2, plotted vorticity displays high frequency transient variations, followed by banded relatively lower frequency variations of the vorticity in Range-1b. In Range-1b, it is possible to see coherent vortices inside the cavity. However, such structures at the core are highly transitory and the time series shows the decay of the signal near the terminal time of Range-1b, the vorticity fluctuation reduces and settles down to a steady value and which is maintained throughout in Range-2. This period is followed by Range-3a, where the vorticity variation displays growth and which is presumably due to linear temporal instability. Finally, in Range-4 one notices nonlinear saturation of the growth noted in Range-3a. This is the typical variation of vorticity with time for lower Re cases, which are above Re_{cr1}.

For such a time series shown in Fig. 2, the linear growth in Range-3a is followed by nonlinear saturation in Range-4 and has often been modeled by Stuart-Landau equation. An objective discussion on applicability of this model is given in [38]. Results obtained by high accuracy solution of time-dependent NSE in Range-2 and that is strictly obtained as solution of steady NSE may not match. Due to this, in the following linearly unstable range, solutions obtained by time-dependent NSE in Range-3a would also not necessarily be the same, which is obtained from the eigenvalue analysis of steady NSE solution. Also, the mismatches in Ranges-2 and -3a, can be due to differences in accuracy of numerical methods employed. The steady state solution obtained in the unstable range is essentially due to the diffusive nature of numerical methods. Such steady solutions have been reported for a high Reynolds number of 20000 [6, 14]. The sensitive dependence of solution of a nonlinear dynamical system to initial condition (here the equilibrium state obtained by two ways) is well known and for fluid dynamical system governed by NSE is recorded in the literature [36]. The Range-4 is where the dynamical system settles down to its limit cycle. We shall note later that the transition from Ranges-2 and -3a to Range-4 can be quite complicated, punctuated by intermediate quasi-equilibrium states which suffer instabilities to take the system to newer equilibrium state. This will be discussed again with respect to higher Re cases.

One of the major aspects of the work reported by Sengupta *et al.* [26, 27] is the multi-modal frequency spectrum of the flow inside LDC for $Re = 10000$. It has been noted that with the use of NCCD scheme, the aliasing error near the top right corner is held in control and only five distinct frequencies are noted in the spectrum for $Re = 10000$. In contrast, when another combination of compact schemes were used for the same problem, the spectrum was seen to be broad-band with presence of fluctuations at multiple scales. This difference between the two methods is due to better diffusion discretization by NCCD scheme [27, 36]. In the present exercise, the same method has been used to track accurately the phenomenon of multiple Hopf bifurcations in the range of Reynolds number: $8000 \leq Re \leq 12000$ and the associated dynamics. For the flow in the range: $8000 \leq Re \leq 8660$, the flow remains steady and would be of lesser interest to us, obtained using (257×257) grid.

In various frames of Fig. 3, we depict vorticity time series at point ($x = 0.95$, $y = 0.95$) for different Re from 8660 onwards. The time series for $Re = 8660$ only displays Ranges-1a, -1b and -2 for the simulation performed up to $t = 2000$. However, for $Re = 8670$, one notices all the ranges shown in

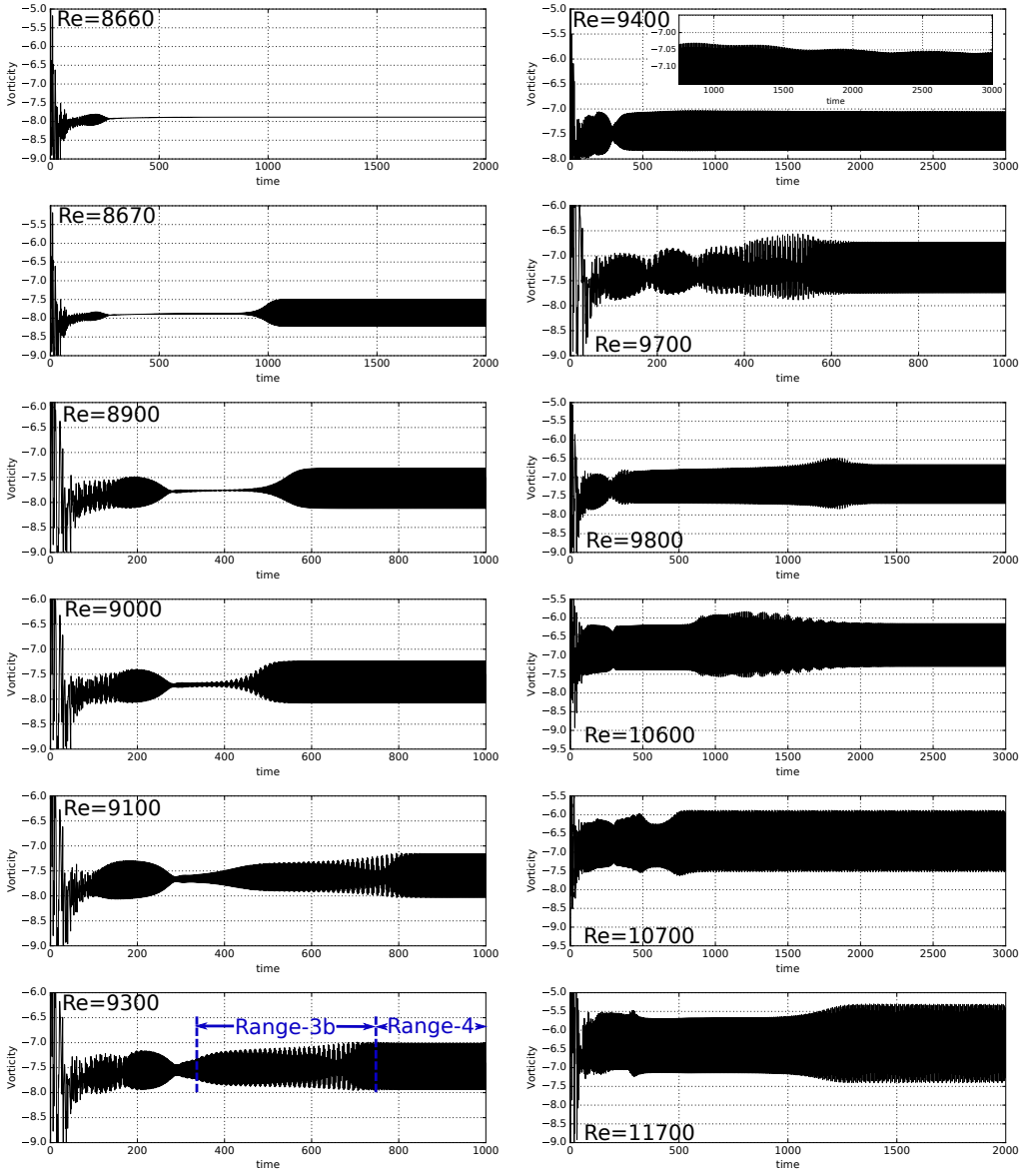

Figure 3: The vorticity time series for a point located at $x = 0.95$, $y = 0.95$, near top right corner for the displayed Reynolds numbers, obtained from solution of unsteady Navier-Stokes equation.

Fig. 2. This implies that the first critical Hopf bifurcation occurs in between these two Reynolds numbers. As Re increases, one notices that the Range-2 shrinks, i.e., the time over which flow remains steady decreases, before being destabilized. This steady state (an equilibrium solution) is unstable, and the flow suffers a temporal instability. For $Re = 8900$, the apparent steady state actually consists of low amplitude oscillations and the flow suffers temporal instability, which can be studied by Floquet theory [5], provided this solution strictly periodic having a single frequency. For such periodic equilibrium flow the eigenvalue analysis for steady flow, as in [6, 30, 16] is not possible. However, the spectrum of periodic solutions are populated with more than one incommensurate frequencies and Floquet analysis is not an option. Thus to avoid such complexities of linear instability studies, we advocate high accuracy solutions of unsteady NSE, as has been practiced also in the literature [8, 18, 19, 26, 27, 38] and here.

With increase in Re above 8800, one notices that the onset of Range-3a also advances, which is noted by comparing the frames in Fig. 3. The Ranges-1a and -1b are seen to change at a slower rate with increase in Re. Also, in the time series for $Re = 9000$ onwards, one notices significant modulations during the growth and nonlinear saturation stages of the vorticity evolution. For $Re = 9100$ onwards, one notices that the Range-2 is completely absent, implying that the flow does not achieve steady state at all. The temporal growth starts from the transient stage (Range-1) itself, for $Re = 9100$. For such cases, eigenvalue analysis of steady state [6, 16, 30] is of no value. This situation is further compounded by multi-modal interactions, as seen for $Re = 9000$ with distinct wave-packets forming. Intensification of modulations and their extension in nonlinear saturation stage is also noted for $Re = 9300$. This is a new unreported instability for LDC flow, which starts from the nonlinear modulation stage and will be referred to as secondary instability henceforth, while the time extent is marked as Range-3b. The demarcation between early transient stage and regular temporal growth stage is visible as a neck formation in the time series near $t = 300$, for $Re = 9100$ onwards. One of the visible signature of the dynamical system having reached a stable equilibrium state is the presence of constant amplitude limit cycle beyond $t = 700$ onwards for $Re = 9300$. We have already noted that depending upon Re, one may or may not see the presence of the five ranges indicated in Fig. 2 for $Re = 9100$.

The marked secondary nonlinear instability is obtained here by high accuracy solution of NSE using NCCD scheme [26, 27]. Even if linear instability

were to be a valid option in the earliest phase in Range-3a, one cannot resort to normal mode analysis [12, 21], since the visible modulation is due to multi-modal interactions. In case of single mode being present during the growth phase, one can use Stuart-Landau equation [24, 40] and explain the nonlinear saturation noted in Range-4, as due to self-interaction only. A theoretical approach to multi-modal interactions has been advanced [23, 35], where the eigenfunction expansion formalism proposed by Eckhaus [13] has been utilized to derive the more general Stuart-Landau-Eckhaus (SLE) equation [23, 35]. SLE equation is a tool to explain the limit cycle stage with multi-modal interactions. Additionally, use of proper orthogonal decomposition (POD) helps one to obtain the instability modes. The governing SLE equations have been used to explain bluff body flow instability, as well as developing reduced order model (ROM) for flow past circular cylinder for low Reynolds numbers in [23, 31].

An exceptional case is also noted for $Re = 9400$, in which the presence of multi-modal interactions is noted even when the computations are carried out till $t = 2000$, as shown in Fig. 3. Only when the computation is extended beyond $t = 3000$, one notices the slow disappearance of modulation. However, the amplitude of the final limit cycle is significantly lower, as compared to neighboring Re cases. This will be further described in presenting multiple Hopf bifurcations. The implications of sustained modulation is explained shortly with the help of spectrum of data after the dynamical system has settled down to an apparent equilibrium state.

With further increase in Re, a secondary instability occurs, as seen for $Re = 9700$, with the final limit cycle setting in before $t = 700$ in Fig. 3. In this case, after Range-1a a series of secondary instabilities are noted, culminating in the final limit cycle very early on. For $Re = 9800$ the first instability is followed by nonlinear action which leads to the amplitude continuously increasing and a single secondary instability is noted around $t = 1200$, which leads to the final limit cycle being firmly established by $t = 1500$. This is an atypical behavior, not seen for lower Re. The vorticity time series for $Re = 9900$, 10000, 10080, 10180 and 10400 (not shown here), follow similar time variation as that of $Re = 9700$. For $Re = 10500$, qualitatively different vorticity dynamics is noted as compared to the case for $Re = 10400$. This time series has resemblance with the case for $Re = 9400$. The vorticity time series for $Re = 10600$ shows qualitatively similar behavior as noted for $Re = 9800$. Above this Reynolds number, computed vorticity field up to $t = 2000$, show continuous modulations in the time series. This is with the

exception of $Re = 11500$ and 11600 cases, for which one notices stable limit cycle after a very small time interval following the formation of neck around $t = 200$.

The described multiple mode interactions and consequent modulations can take a long time (T_{lc}) before the dynamical system settles down to a stable limit cycle. Additionally, this process is very sensitive to the Reynolds number as one can infer from Fig. 4. Indeed T_{lc} behaves irregularly during the very short range $10000 \leq Re \leq 10400$ that is displayed here.

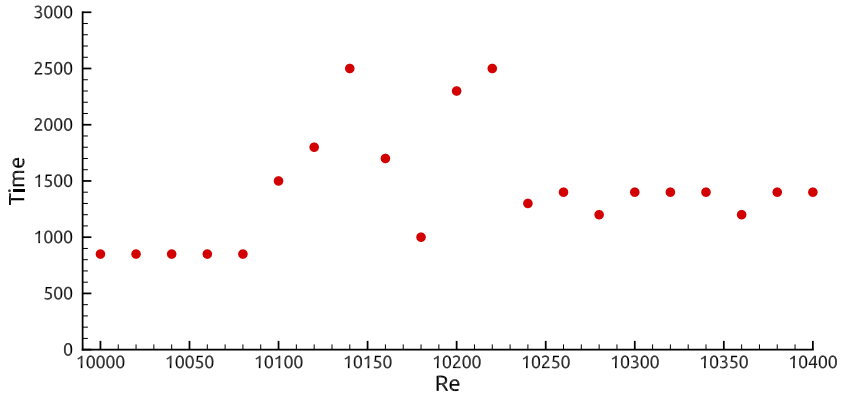

Figure 4: The onset time of final stable limit cycle of the vorticity time series for the displayed Reynolds numbers, with solution shown for the location given by, $x = 0.95$ and $y = 0.95$.

4. Vorticity dynamics and polygonal vortex in LDC

From the time series shown in Fig. 3 for different Re's at the stable limit cycle stage, we have noted the feature of periodicity of the solutions in the final limit cycle. Here, we investigate further about the flow field for $Re = 10300$ to describe the flow evolution in terms of vorticity dynamics. In Fig. 5, we show the vorticity contours inside the cavity at the indicated time instants, while the vorticity time series at $(x = 0.95, y = 0.95)$ is shown as the central panel in Fig. 5, to understand the choice of the time instants.

In the early stages of flow evolution, the inner core develops in conformity with the shape of the cavity, due to the action of the wall jet impinging near the top right corner. Thus, the lighter shaded contours shown in the form of a rounded rectangle, while the inner contour lines morph into a

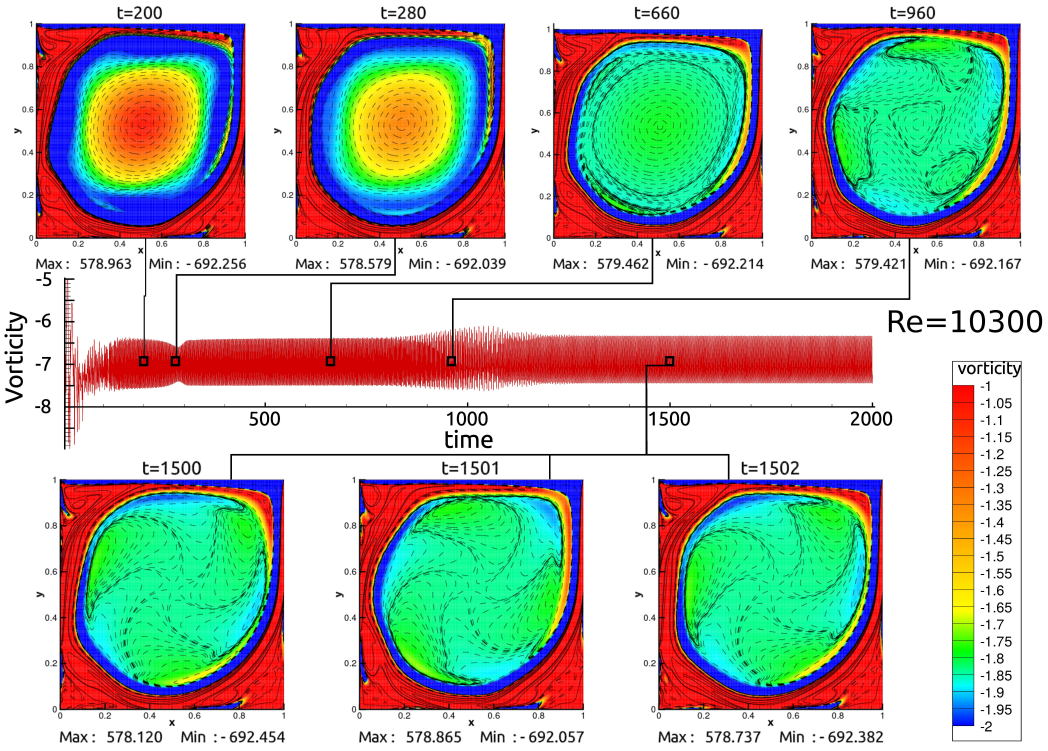

Figure 5: Vorticity contour is shown at different time instants from start till attainment of limit cycle for $Re = 10300$. Time series of the vorticity at point $(0.95, 0.95)$ is shown in the center.

circular shape, as noted at $t = 200$. From the time series, one notes this stage to belong to beyond the early transient, where the coherent motion corresponds to a apparent neutral stage which is followed by decay of the disturbance. This continues up to $t = 280$, when the time series indicate the termination of decay and beyond this time, the disturbance once again grow. The vorticity contours show two distinct layers with sharp gradient and this motion continues, as shown in the frame for $t = 660$, where the gradient is really sharp. In subsequent flow evolution, the outer layer transforms into satellite vortices while the inner core shrinks to the triangular vortex, as noted in the frame for $t = 960$. Such triangular vortices have been shown earlier for $Re = 10000$ [26, 27] and it is noted here also. The time series also indicates that there is no steady state for this flow to perform linear stability analysis, as attempted by other researchers [6, 30]. This helps one to conclude that the

presence of triangular core vortex is essentially due to nonlinear dynamics of the flow field guided by the presence of six gyrating satellite vortices. However, with passage of time the central core vortex looses strength and identity. Thereafter, one notices these six gyrating satellite vortices to rotate about the center of the cavity. This is the terminal state of the limit cycle. One such cycle is shown in the bottom three frames.

5. Multiple Hopf Bifurcation

The vorticity time series described in section 3 indicate different qualitative dynamics for different Re and that in turn is suggestive of multiple bifurcations in the range of computed solutions. Here, we address bifurcations for the LDC flow based on DNS performed following an impulsive start. To do so the limit cycle amplitude is studied first, then the analysis of the frequencies property allows a better comprehension of the underlying mechanisms.

5.1. New Equilibrium State via Stable Limit Cycle

The amplitude of the limit cycle A_e is defined as half of the maximum excursion of the vorticity time-series describing a constant width envelope, by sampling the vorticity at $(0.95, 0.95)$. Different time evolution at the sampling point for different Re are presented in Fig. 3. For some higher Re cases, computed flow field display significant modulation even when the flow is computed up to $t = 2000$ and above. The Stuart-Landau model states that $A_e^2 \propto |(Re - Re_{cr1})|$ for the limit cycle cases with single dominant mode and this is useful for the flow past a circular cylinder approximately. Correspondingly, Fig. 6 displays the plot of A_e^2 as a function of Re for the range $8660 \leq Re \leq 12000$ obtained using a grid with (257×257) points. Unlike the nonlinear dynamical systems for bluff bodies, here the Hopf bifurcation [39] starts very sharply, as shown in Fig. 6, which occurs between $Re = 8660$ and 8670. For flow past a circular cylinder, DNS based Hopf bifurcation studies and corresponding results are given in [23]. Each zoomed view in Fig. 6 shows a segment in which relation between Re and A_e^2 is compared with its linear variation. The linear regression coefficients can be found in Table 1.

In the range $8670 \leq Re \leq 9350$, one can see in Fig 6 that the linear regression fits the data well. This is confirmed by the value of R^2 being really close to 1. The amplitude then suddenly drops around $Re = 9400$, as noted in Fig. 6. To ascertain the correctness of this value, additional

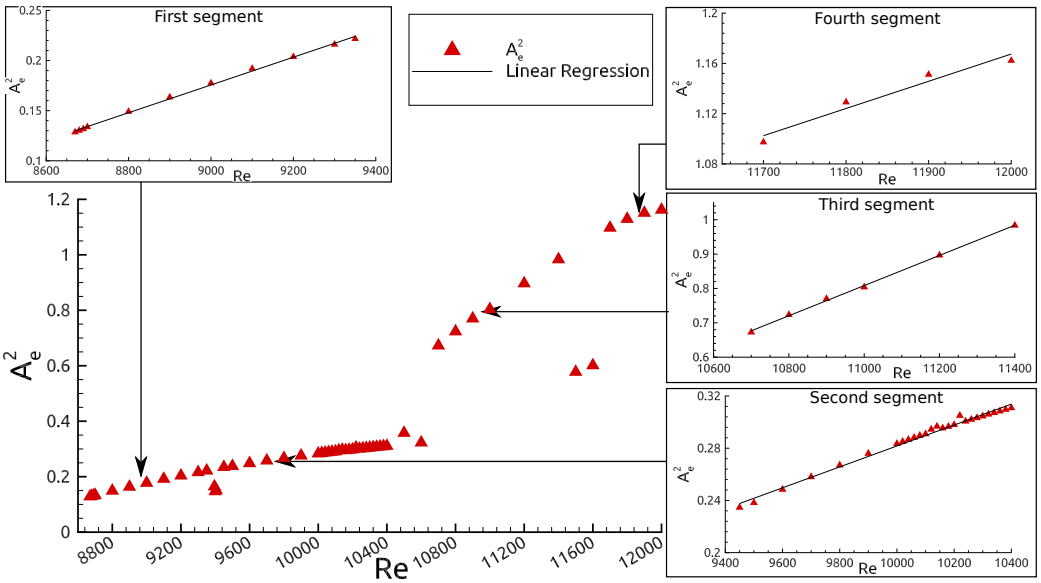

Figure 6: Multiple Hopf-bifurcation shown with respect to the vorticity time series data shown for Fig. 2. All the simulated Reynolds numbers data are used to plot the amplitude of the final stable limit cycle data against Reynolds number.

simulations have been performed for $Re = 9350$, 9395, 9405 and 9450 and all these data are marked in the figure. It is noted that the value for $Re = 9350$ falls on the linear segment shown to the left of $Re = 9400$. For $Re = 9450$, the amplitude belongs to the next linear segment which ends at $Re = 10400$, as shown in Fig. 6 in the second box. However it should be noted that the correlation coefficient is lower on this range, mainly due to its larger extent. Another natural break in the curve is noted between $Re = 10500$ and 10600. Once again a linear segment is plotted for the data points for $Re = 10700$ to 11400. $Re = 11500$ and 11600 show a particular behavior in the higher Re range since A_e^2 values fall abruptly and then the amplitude again rises sharply at $Re = 11700$ defining the fourth bifurcation. A new range up to 12000 is presented in the fourth box of Fig. 6, however the correlation coefficient is low, implying that A_e^2 does not vary linearly with Re.

A similar curve was drawn using the highest amplitude of spectrum (obtained by the FFT of the time series) for each Reynolds number [38]. Also, the simulations have been performed here over a significantly longer time interval, till we obtained the stable final limit cycle. It has been noted [23, 38]

Table 1: Coefficients of linear regression equation of the form : $A_e^2 = aRe + b$ with regression correlation coefficient R.

Segment	a	b	R^2
1	1.384672e-4	-1.070575	0.998
2	8.017815e-5	-0.520059	0.992
3	4.389279e-4	-4.019874	0.999
4	2.166881e-4	-1.432799	0.956

that the presence of such discontinuities is indicative of multiple Hopf bifurcations in (A_e^2, Re)-diagram, as in Fig. 6. The fact that the flow behaves qualitatively different in different range of Re is indicative of discrete change in A_e^2 with respect to Re, as indicated in Fig. 6. Along with such changes in the physical plane, one would expect to notice qualitative changes of the spectrum of the time series already shown in Fig. 3. These are now shown in Fig. 7, testifying the qualitative changes in the flow field following the appearance of a new bifurcation. From Fig. 6 and Tab. 1, one can infer the presence of four such Hopf bifurcations. In order to provide a better understanding of the phenomena at work here, the next sub-section will focus on spectral analysis of the vorticity time series at point $(0.95, 0.95)$.

5.2. Frequency Spectrum Analysis

In Fig. 7, we show few Fourier transforms of the time series shown in Fig. 3. Fourier analysis is applied over the last 100 cycles, i.e., after the stable limit cycle is reached. In order to provide accurate plots, the average on that time span has been removed from each time series. It is clear that for $Re = 8800$, the dynamics is governed mostly by three harmonics, with subsequent ones being more than a decade lower than the lowest of these top three frequencies, as noted in Fig. 7. Other higher Re cases display similar spectra for $Re = 8800$ to 9300 (not shown here). The displayed harmonics for different Re in this range, also show the primary modal frequencies to remain constant up to $Re = 9300$, as shown in Tab. 2 (the features of which is discussed in details later). In the range of Re around 9400, the fundamental and higher harmonics display variations of frequencies that is typically different with two lower peaks appearing on each side of a central spike and there are more than three spikes, including one with very low

frequency. Also the spectrum for $Re = 9400$ in Fig. 7 shows rightward shift of all the major harmonics. As noted in Fig. 6, the flow behavior above $Re \approx 9450$ resembles flows noted for lower post-critical Reynolds numbers. This is clearly seen in Fig. 7 for $Re = 9800$ with six peaks in the spectrum. This is the state of flow behavior till $Re = 10400$, these frequencies revert back to the lower constant value, that was noted for up to $Re = 9300$; with the number of peaks increasing, as shown in Fig. 7 for $Re = 9800$. For the higher $Re = 10700$ shown in Fig. 7, one notices a large numbers of spectral peaks with more than one dominant comparable peaks. This feature of two dominant modes are noted up to $Re = 11400$. We also remark that unlike the spectra for lower Re cases, these higher Re cases have many peaks in the spectrum. The spectrum for $Re = 11500$ and 11600 (not shown here) again displays very clean spectrum with very few peaks, as was noted for $Re = 8800$ to 9300. For $Re = 11700$ and higher (not shown here), once again the spectrum represent two dominant modes, with larger number of peaks present. The only difference between this case and the one for $Re = 11400$ is that the peak amplitude is higher for the higher frequency, as shown in Fig. 7.

5.3. Phase Portrait Analysis

For the 2D LDC flow, the governing NSE in primitive variables are given by two evolution equations for velocity components (u, v), apart from the mass conservation equation. Thus, the phase portrait of this dynamical system should ideally be given in the (u, v)-plane with time as the parameter. However in our approach we have solved NSE in the (ψ, ω)-formulation thereby exactly satisfying the mass conservation equation. Also, this formulation avoids the pressure-velocity coupling problem. Thus, we propose to depict the phase space portrait by plotting vorticity and its time rate in Fig. 8 for the sampling point at $(x = 0.95, y = 0.95)$. The time series depicting the history of vorticity evolution for these cases have been already shown in Fig. 3. We have plotted the phase space portrait for the indicated time ranges, where the time series indicates the existence of stable limit cycle-like behavior. This is confirmed by the phase space portrait for the relatively lower post-critical Re values. Except for $Re = 9400$ case, all the other three cases for $Re = 8800$, 10000 and 10300 show almost identical limit cycles. Excursion of ω about the mean value is almost similar and there is a characteristic dip in the limit cycle in all the three cases, except for $Re = 9400$, for which the phase portrait almost shows oblong oval shape. The width of

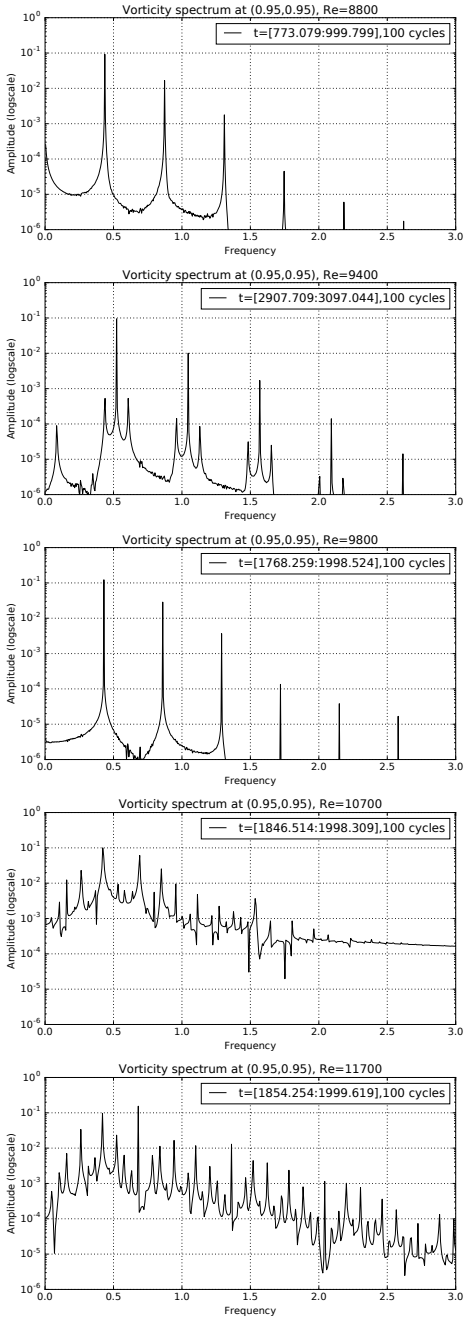

Figure 7: The frequency spectrum of the vorticity time series shown for all the simulated Reynolds numbers, for the solution obtained from unsteady Navier-Stokes equation and the data are for $x = 0.95$ and $y = 0.95$.

Table 2: Frequencies of the six leading harmonics (only shown if amplitude (given in parenthesis) is larger than 10^{-4}). Asterisk (*) for the $Re = 9400$ and $Re = 10500$ indicates the presence of doublet peaks accompanying the main spike. Shaded lines indicate that many peaks are found in the Fourier analysis, only the first six in amplitude are given.

Re	F_1	F_2	F_3	F_4	F_5	F_6
8670	0.437 (8.61e-2)	0.874 (1.44e-2)	1.312 (1.46e-3)	1.749 (3.83e-5)	2.186(4.14e-6)	2.623 (1.20e-6)
8680	0.437 (8.66e-2)	0.874 (1.46e-2)	1.311 (1.49e-3)	1.748 (3.90e-5)	2.186 (4.02e-6)	2.623 (1.16e-6)
8690	0.437 (8.71e-2)	0.874 (1.48e-2)	1.311 (1.51e-3)	1.748 (3.97e-5)	2.185 (3.86e-6)	2.622 (1.18e-6)
8700	0.437 (8.76e-2)	0.874 (1.49e-2)	1.311 (1.54e-3)	1.749 (3.86e-5)	2.186 (4.50e-6)	2.627 (1.56e-6)
8800	0.437 (9.23e-2)	0.873 (1.66e-2)	1.310 (1.78e-3)	1.746 (4.50e-5)	2.183 (6.00e-6)	2.620 (1.74e-6)
8900	0.436 (9.64e-2)	0.871 (1.81e-2)	1.307 (2.00e-3)	1.742 (5.13e-5)	2.178 (6.00e-6)	2.614 (2.33e-6)
9000	0.435 (1.00e-1)	0.870 (1.95e-2)	1.305 (2.22e-3)	1.740 (5.66e-5)	2.174 (8.26e-6)	2.609 (3.00e-6)
9100	0.435 (1.04e-1)	0.871 (2.10e-2)	1.306 (2.47e-3)	1.739 (6.29e-5)	2.173 (9.89e-6)	2.608 (4.88e-6)
9200	0.434 (1.07e-1)	0.867 (2.22e-2)	1.301 (2.65e-3)	1.740 (6.89e-5)	2.168 (1.29e-5)	2.602 (5.51e-6)
9300	0.433 (1.10e-1)	0.866 (2.35e-2)	1.299 (2.86e-3)	1.733 (7.55e-5)	2.166 (1.62e-5)	2.599 (7.39e-6)
9350	0.433 (1.12e-1)	0.866 (2.41e-2)	1.299 (2.95e-3)	1.731 (7.94e-5)	2.164 (1.85e-5)	2.597 (7.91e-6)
9395	0.085 (1.12e-3)	0.523* (9.30e-2)	1.046* (9.74e-3)	1.569* (1.61e-3)	2.092* (1.29e-4)	2.615 (1.11e-5)
9400	0.085 (8.91e-5)	0.523* (9.45e-2)	1.046* (1.01e-2)	1.569* (1.70e-3)	2.091* (1.40e-4)	2.614 (1.42e-5)
9405	0.086 (1.08e-4)	0.523* (9.48e-2)	1.046* (1.02e-2)	1.568* (1.72e-3)	2.091* (1.41e-4)	2.614 (1.50e-5)
9450	0.432 (1.14e-1)	0.865 (2.53e-2)	1.297 (3.16e-3)	1.730 (8.63e-5)	2.162 (2.16e-5)	2.594 (8.93e-6)
9500	0.432 (1.15e-1)	0.864 (2.58e-2)	1.296 (3.22e-3)	1.728 (9.30e-5)	2.160 (2.41e-5)	2.591 (1.05e-5)
9600	0.431 (1.18e-1)	0.862 (2.68e-2)	1.294 (3.38e-3)	1.725 (1.05e-4)	2.156 (2.86e-5)	2.587 (1.25e-5)
9700	0.431 (1.20e-1)	0.861 (2.78e-2)	1.292 (3.53e-3)	1.722 (1.20e-4)	2.153 (3.31e-5)	2.583 (1.43e-5)
9800	0.430 (1.23e-1)	0.860 (2.87e-2)	1.290 (3.67e-3)	1.720 (1.35e-4)	2.150 (3.81e-5)	2.580 (1.65e-5)
9900	0.429 (1.25e-1)	0.858 (2.94e-2)	1.287 (3.78e-3)	1.716 (1.61e-4)	2.145 (4.32e-5)	2.574 (1.75e-5)
10000	0.429 (1.27e-1)	0.857 (3.02e-2)	1.286 (3.89e-3)	1.714 (1.75e-4)	2.143 (4.88e-5)	2.572 (2.07e-5)
10100	0.428 (1.29e-1)	0.856 (3.09e-2)	1.284 (3.98e-3)	1.712 (1.99e-4)	2.140 (5.52e-5)	2.568 (2.32e-5)
10200	0.427 (1.31e-1)	0.855 (3.16e-2)	1.282 (4.05e-3)	1.709 (2.27e-4)	2.136 (6.25e-5)	2.564 (2.55e-5)
10300	0.427 (1.33e-1)	0.853 (3.22e-2)	1.280 (4.11e-3)	1.706 (2.57e-4)	2.133 (7.02e-5)	2.560 (2.83e-5)
10400	0.426 (1.34e-1)	0.852 (3.27e-2)	1.278 (4.15e-3)	1.704 (2.89e-4)	2.130 (7.81e-5)	2.556 (3.12e-5)
10500	0.167 (6.79e-5)	0.597* (1.37e-1)	1.191* (6.50e-3)	1.786* (3.02e-3)	2.384* (2.48e-4)	2.980 (2.17e-6)
10600	0.425 (1.38e-1)	0.849 (3.36e-2)	1.274 (4.21e-3)	1.698 (3.60e-4)	2.123 (9.56e-5)	2.547 (3.68e-5)
10700	0.159 (1.29e-2)	0.265 (2.71e-2)	0.424 (1.27e-1)	0.530 (1.04e-2)	0.689 (7.09e-2)	0.849 (2.74e-2)
10800	0.160 (1.14e-2)	0.264 (2.86e-2)	0.424 (1.24e-1)	0.528 (1.08e-2)	0.688 (8.20e-2)	0.848 (2.55e-2)
10900	0.160 (1.13e-2)	0.264 (3.09e-2)	0.424 (1.17e-1)	0.528 (1.39e-2)	0.688 (9.36e-2)	0.848 (2.05e-2)
11000	0.160 (1.08e-2)	0.264 (3.19e-2)	0.423 (1.18e-1)	0.527 (1.45e-2)	0.687 (1.01e-1)	0.846 (2.20e-2)
11100	0.264 (3.43e-2)	0.423 (1.12e-1)	0.527 (1.61e-2)	0.687 (1.11e-1)	0.846 (1.81e-2)	0.950 (1.17e-2)
11200	0.263 (3.48e-2)	0.422 (1.12e-1)	0.526 (1.78e-2)	0.686 (1.17e-1)	0.845 (1.79e-2)	0.949 (1.24e-2)
11300	0.263 (3.39e-2)	0.422 (1.05e-1)	0.526 (2.02e-2)	0.685 (1.29e-1)	0.844 (1.50e-2)	0.947 (1.35e-2)
11400	0.262 (3.44e-2)	0.421 (1.07e-1)	0.525 (2.18e-2)	0.684 (1.32e-1)	0.842 (1.54e-2)	0.946 (1.36e-2)
11500	0.587 (1.94e-1)	1.175 (7.91e-3)	1.762 (4.26e-3)	2.349 (6.39e-4)	2.937 (1.17e-5)	
11600	0.586 (1.98e-1)	1.173 (8.32e-3)	1.759 (4.47e-3)	2.346 (6.89e-4)	2.932 (1.40e-5)	
11700	0.261 (3.39e-2)	0.420 (9.64e-2)	0.523 (2.33e-2)	0.681 (1.54e-1)	0.942 (1.65e-2)	1.362 (1.29e-2)
11800	0.261 (3.29e-2)	0.419 (9.23e-2)	0.522 (2.20e-2)	0.680 (1.61e-1)	0.941 (1.71e-2)	1.360 (1.43e-2)
11900	0.261 (3.15e-2)	0.420 (8.70e-2)	0.521 (1.80e-2)	0.679 (1.68e-1)	0.939 (1.70e-2)	1.358 (1.54e-2)
12000	0.260 (3.03e-2)	0.418 (7.96e-2)	0.521 (1.79e-2)	0.678 (1.76e-1)	0.939 (1.84e-2)	1.357 (1.76e-2)

the limit cycle is slightly wider for $Re = 9400$, due to the typical frequency spectrum shown in Fig. 7 with dominant spikes accompanied by side-bands on either side. As the second dominant cluster in the spectrum is one decade higher than the global maximum for this case, explains the near-oval shape of the phase space portrait. In contrast, for the other three Re cases, the global maximum and the nearest higher peaks are not widely separated and such multi-modal behavior, whose mutual interaction can reduce $\frac{d\omega}{dt}$ for a particular combination of phase (i.e., at a particular time) during each cycle.

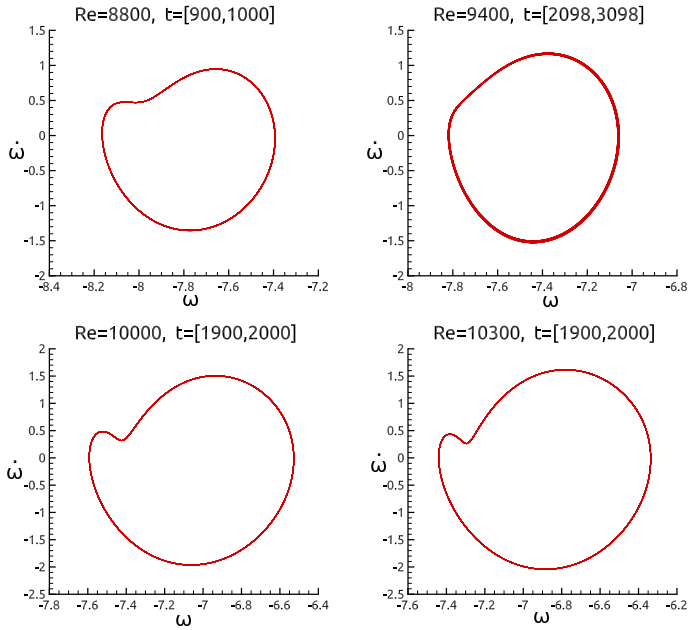

Figure 8: Phase portrait of the vorticity $(\omega, \dot{\omega})$ at $(0.95, 0.95)$ once the last 100 time interval for $Re = 8800$, 9400, 10000, 10300. Trajectories are closed since stable limit cycle has been reached.

5.4. Multi-periodic State

Beyond the third Hopf bifurcation, i.e., beyond $Re = 10600$, the flow field changes qualitatively, as noted from the time series in Fig. 3 and the frequency spectrum in Fig. 7 for Re = 10700. The time series is characterized by the significant modulation noted for time greater than $t \approx 1000$. The same characteristic is noted better in the spectrum, where one can see many dominant frequencies of comparable magnitude. Presence of multiple time

scales lead to vorticity contours, as shown in top frames of Fig. 9 for $Re = 11000$ and $Re = 12000$ which shows the irregular six gyrating vortices and their center is not aligned with the geometric center of the cavity. The irregularity of gyrating vortices is more pronounced at the higher Reynolds number case. However, this aspect is seen very graphically from the phase space portrait shown in the bottom frames of Fig. 9. The lower Re case show distinct limit cycles with larger basin of attractor and quasi-periodicity of the flow field is evident. However, for $Re = 12000$ the phase space portrait is characterized by large continuous basin of attractor with its appearance given by a Mobius strip.

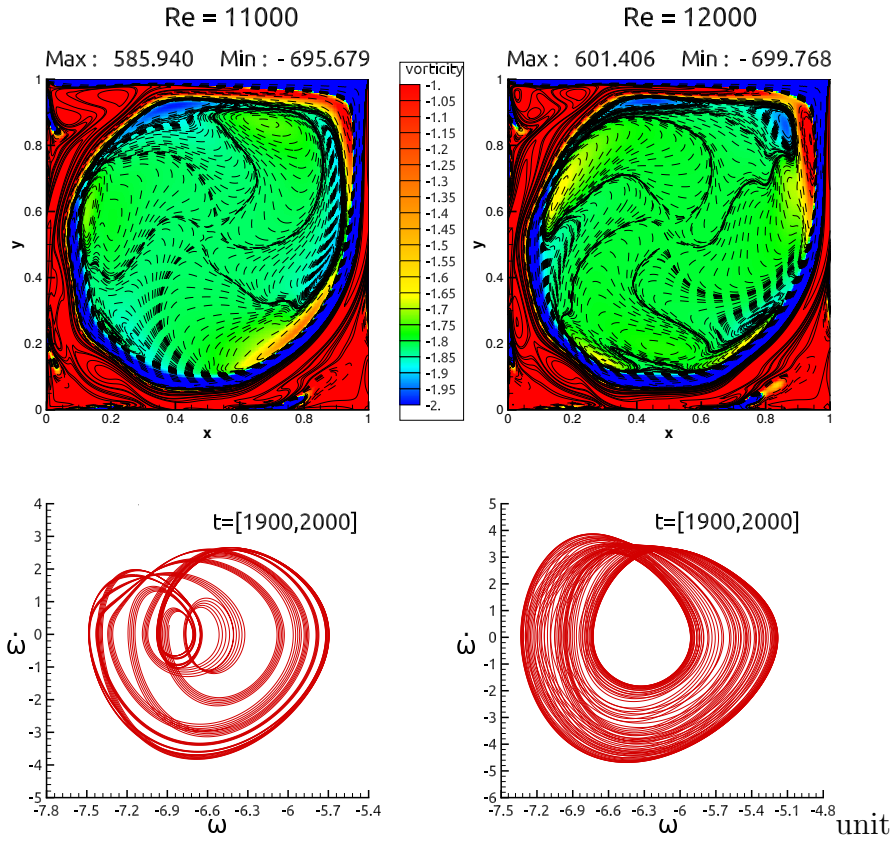

Figure 9: Two examples of unstable limit cycle for $Re = 11000$ (left) and $Re = 12000$ (right). Vorticity contour plot is shown in the first row at $t = 2000$ and phase portrait in the second.

6. Numerical sensitivity of the problem

The singular LDC problem is very sensitive to numerical setup. In this section we discuss two major issues affecting the solution, namely start-up conditions and grid sensitivity of our numerical method.

6.1. Influence of grid resolution

Computations have been performed on two different grids, i.e., (257×257) and (513×513), in order to assess effects of grid on the simulation. Figure 10 displays time series for two different grids which clearly behave differently. On the one hand, the coarse grid exhibit a secondary instability around $t = 1200$, that leads to the final limit cycle. Because of finer wall resolution, calculated wall vorticity is higher for the finer grid calculation. Yet, the numerical excitation caused by sources of error is lower for the finer grid. As a consequence, both the mean and fluctuation of disturbance vorticity is lower for the finer grid, which causes upward shift of the mean vorticity line, i.e., reduction of mean vorticity of disturbance. No secondary instability is seen for the finer grid and still a similar limit cycle is reached with marginal difference in amplitude and frequency of the fluctuating component of vorticity. Moreover, final state is stable for $Re \leq 9400$ when computations are carried on the finer (513×513) grid, i.e., $Re_{cr1} \in [9400, 9450]$. It emphasizes that the flow is driven by the receptivity aspect of the problem, with coarser grid (and less accurate numerical methods) having larger excitation due to implicit error, shows early onset of first Hopf bifurcation. This will be further discussed in the subsection 6.3.

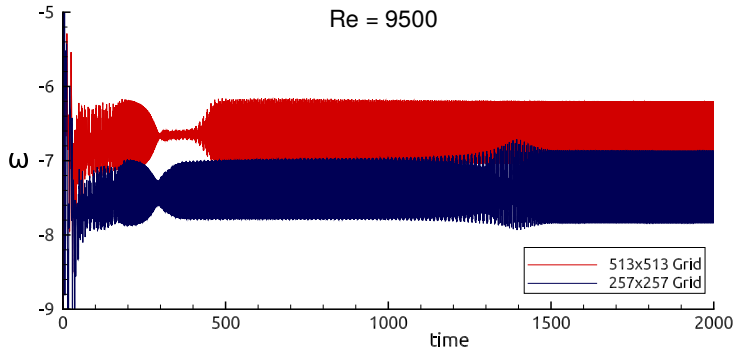

Figure 10: Vorticity time series are shown for $Re = 9500$ for two different grid spacing 257×257 and 513×513.

6.2. Effect of start-up conditions

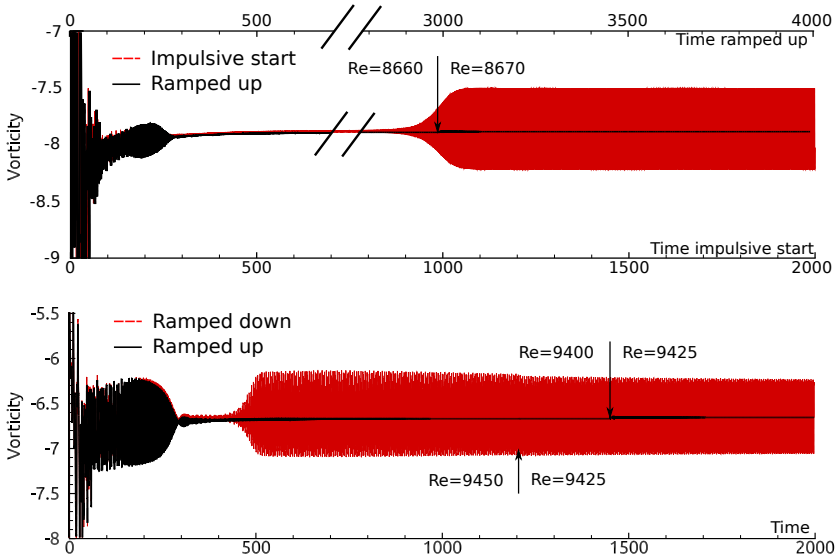

Figure 11: The figure in top shows $Re = 8670$ being initialized by impulsive start-up (dashed) and ramp up from the limit cycle solution of $Re = 8660$ at t=2000. The bottom figure shows result with the fine grid of (513×513) size for $Re = 9425$ computed from the limit cycle solutions of $Re = 9400$ (solid) and $Re = 9450$ (dashed).

The top sub-figure of Fig. 11 depicts the time series stored for $(0.95, 0.95)$ on (257×257) grid for $Re = 8670$ with two different initial conditions. The dashed line corresponds to the usual impulsive start whereas the solid line corresponds to the solution obtained by ramping up from $Re = 8660$ equilibrium solution. We note that the projected solution starting from lower Re remains quiescent (negligibly small variations), while the solution started impulsively shows non-zero values at the sampling point.

The bottom sub-figure of Fig. 11 is for (513×513)-grid in the vicinity of the bifurcation obtained for this grid near $Re = 9400$. Two different start-up cases are presented : (a) when the solution is obtained for $Re = 9425$ starting from an equilibrium solution obtained for $Re = 9450$ and (b) when the initial solution is projected from the case of $Re = 9400$. For the latter case, the vorticity field does not show any disturbance, while the former case shows significant disturbance vorticity. This justifies, *a posteriori*, the use of impulsive start-up which is known to excite all modes of oscillation simultaneously by equal magnitude.

6.3. Computational bifurcation analysis: Is there a universal critical Reynolds number for primary bifurcation?

In introduction, we have noted that different researchers have reported different critical Re_{cr1}, ranging from $7763 \pm 2\%$ to 10,500, with a marked clustering around Re_{cr1} in the vicinity of 8000. For example, $Re_{cr1} = 8018$ in [3] and 8031.93 in [32]. Cazemier *et al.* [11] reported Re_{cr1} at 7972, while Bruneau and Saad [8] suggested this to be in the range of $8000 \leq Re_{cr1} \leq 8050$. Sengupta *et al.* [38] have described multiple Hopf bifurcations, showing the first one at 7933 and the second at 8187, using uniform (257×257) grid, with bifurcation diagram drawn using the amplitude of the primary mode only. In [28], this value is reported at $7987 \pm 2\%$. In light of these scattered values, we furthermore investigated why the present simulation using CCD scheme using the uniform (257×257) grids produces Re_{cr1} in the narrow range of 8660 and 8670, when no explicit excitation is applied.

One of the attributes of the used CCD scheme is its near-spectral accuracy and it has been reasoned in [26, 27], the trigger for the unsteadiness is the aliasing error originating near the top right corner of the LDC, while the truncation, round-off and dispersion error is extremely negligible [44, 45]. To circumvent the issue of lower numerical excitation in the present work (which is based on the method in [26, 27, 38]), we position a pulsating vortex of the form at a location $r_0 = (0.015625, 0.984375)$ whose spread is defined by the exponent α,

$$\omega_s = A_0(1 + \cos(\pi(r - r_0)/0.0221)) \sin(2\pi f_0 t) \quad \text{for } (r - r_0) \leq 0.0221$$

where in the presented results here we have taken $f_0 = 0.41$ for different amplitude cases. For $Re = 8660$ and below, we start with $A_0 = 1.0$. Once the excitation is started, one notices the vorticity to grow and saturate to a limit cycle. Once the limit cycle is set up, the excitation source is switched off and yet the limit cycle continues. The saturated limit cycle amplitude for decreasing Reynolds numbers are shown in Fig. 12 along with the unexcited cases (shown by hollow triangle facing towards left, up to $Re = 8670$) for the sampling point at $x = 0.95, y = 0.95$. The excited cases with $A_0 = 1.0$ and $f_0 = 0.41$ are shown with filled triangles facing towards right, up to $Re = 8030$. Below this Reynolds number value, the vortex source strength has to be increased to obtain self-sustained limit cycle, as shown by the upright hollow triangle for $Re = 8025$ and $A_0 = 10.0$.

Below this Reynolds number, increasing strength of pulsating vortex does

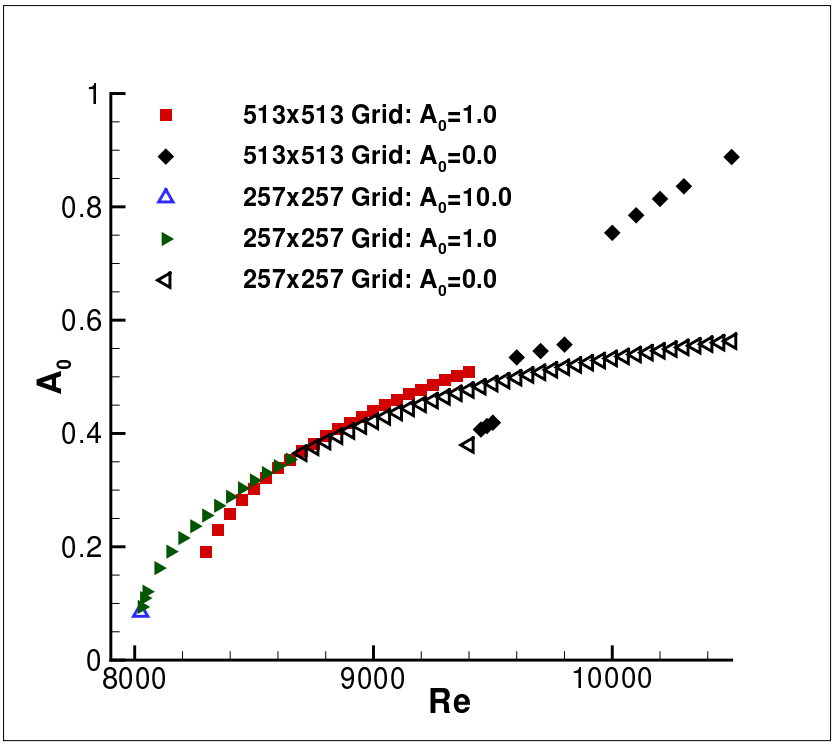

Figure 12: The extended bifurcation diagram obtained using the pulsating vortex source near the top left of the LDC. It is noted that as Reynolds number decreases, the imposed pulsating vortex strength is to be increased. For $Re = 8020$, no excitation with higher amplitude produces stable final limit cycle.

not produce stable limit cycle. We note that the imposed vortical perturbation in the limiting amplitude case of $A_0 = 10.0$, constitute a perturbation level of around 20 percent of the maximum vorticity in the domain. Thus, this computational exercise indicate that the first critical Reynolds number (Re_{cr1}) lies between 8020 and 8025 and similar range of the value noted by many researchers as noted in the previous paragraph. The present DNS does not require linearization or making assumptions pertaining to growth in time or space.

The fact that the flow in LDC cannot be made unsteady for $Re = 8000$ is demonstrated in Fig.13. In the top frame, the vorticity time series are shown at the sampling point $(x = 0.9922, y = 0.9922)$ for the indicated Re values, which is decreased by a step of 100, starting with $Re = 8400$ up to

8100, for $A_0 = 1.0,\ f_0 = 0.41$. For this amplitude of excitation, one notices a modulated time series, due to mutual interference of the natural frequencies with the imposed time scale. However, when the excitation is switched off at $t = t_s$, a pure and stable limit cycle is obtained in Fig.13(a), up to $Re = 8100$. For the case of $Re = 8000$, the withdrawal of excitation causes the vorticity time series to decay. In frames (b) to (d), the results for the cases are shown for which the pulsating vortex amplitude is increased to $A_0 = 1$, 2 and 10 for $Re = 8000$, with the frequency kept the same at $f_0 = 0.41$. When the amplitude of excitation is doubled to 2.0, the modulated time series is noted, and thereafter the exciter is switched off at t_s. One notices that beyond t_s, with exciter switched off, the flow inside the LDC approaches a steady state. For the case of $A_0 = 10.0$, when the exciter is turned on, instead of the modulated time series, one notices a wide-band response of the vorticity field without any perceptible limit cycle. Even with such large excitation amplitude for such a Re, when the excitation is switched off at t_s, one notices the vorticity field to be quiescent again in a short time. Thus, this value of $Re = 8000$ shows that the flow is stable, even for a large perturbation, which is of the order of 20% of the maximum vorticity in the domain.

Finally in Fig.14 we show results for $Re = 8500$, for different amplitude of pulsating excitation source. For this Reynolds number we note the causation of stable limit cycle for $A_0 = 0.06$, while it goes back to steady state for $A_0 = 0.04$. It is also equally important to note that for all the amplitudes of excitation, the final limit cycle has always the same amplitude. This indicates that the present analysis produces results which are invariant of the way one excites the flow. It also shows that this flow shows the receptivity of the flow field, as has been highlighted earlier for external vortex dominated flow in [35].

7. Summary and Conclusion

Flow inside a LDC is shown to display multi-modal behavior following first Hopf bifurcation with varying Re, depending upon the discretization schemes. DNS following impulsive start, is used to show initial temporal growth followed by nonlinear saturation of disturbance. Researchers have reported different value of Re_{cr1} using direct simulation of Navier-Stokes equation. This approach differs from bifurcation studies using global instability study of an equilibrium flow due to adopted nonlinear approach and not restricting the analysis to temporal instability only. Here, flow

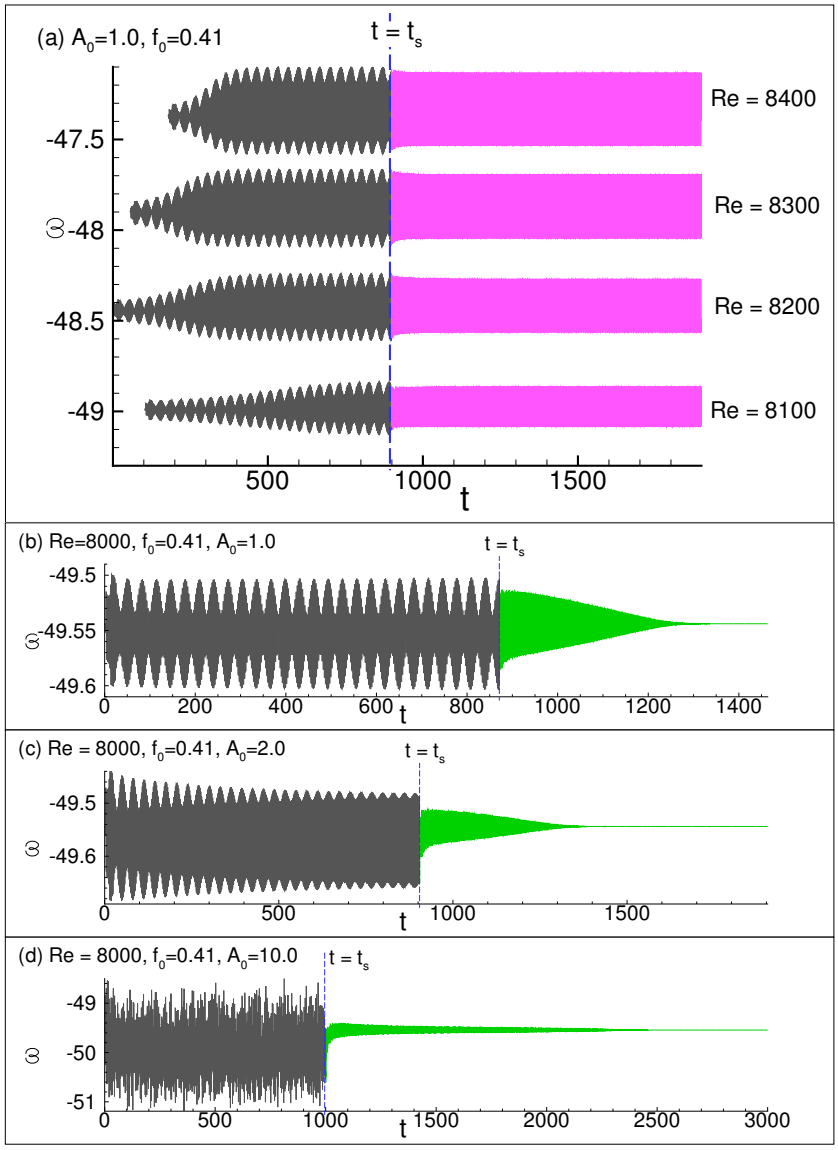

Figure 13: The vorticity time series at the indicated sampling station at $x = 0.9922$, $y = 0.9922$, for the indicated Reynolds numbers, for which stable limit cycle is obtained by the pulsating vortex source near the top left of the LDC.

in LDC is investigated using high accuracy NCCD scheme for DNS using stream function-vorticity, (ψ, ω)-formulation for the range of Reynolds num-

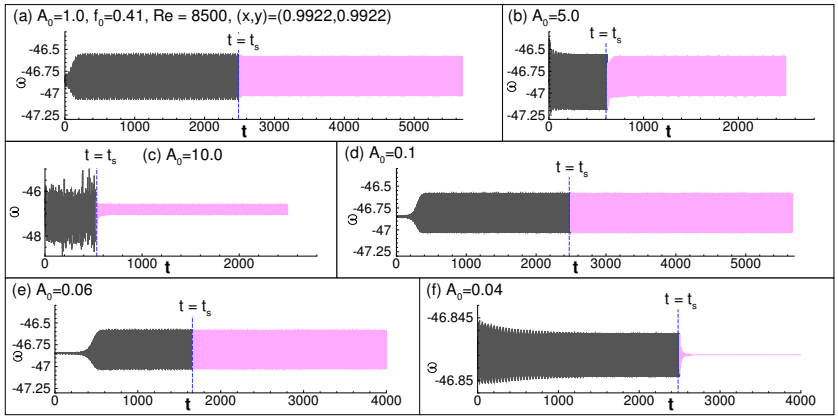

Figure 14: The vorticity time series at the sampling station for $Re = 8500$ shown for cases with varying amplitude of excitation, to find the limiting amplitude for which stable limit cycle is obtained by the pulsating vortex source near the top left of the LDC.

bers, $8000 \leq Re \leq 12000$.

The accuracy aspect of DNS adopted here has been shown conclusively via (a) demonstration of a very weak transient polygonal core vortex surrounded by relatively stronger gyrating vortices, which appear as a constellation, as shown earlier in [26, 27]. This requires extreme accuracy of resolving convection and diffusion terms, otherwise the created aliasing error affects the numerical stability of the method and also maintaining the complex equilibrium in creating the constellation and (b) the value of the first critical Reynolds number, Re_{cr1} depends strongly upon the error dynamics of the adopted discretization scheme for a model equation [36]. One of the major achievements of the present work is to show that Re_{cr1} can be further reduced by explicit excitation for very high accuracy numerical schemes. Thus, we distinguish between excited and unexcited LDC flow here. This difference is described in details in section 6.3, where it is established that the delay of onset for Re_{cr1} is an attribute of accuracy of the present method, and not due to excessive numerical diffusion of the methods, as in [6, 8, 14, 17].

The vorticity evolves here for the unexcited cases, as in Fig. 5, where one sees the presence of transient triangular vortex at the core is unsteady for $Re > Re_{cr1}$. Dynamics is further studied by time series analysis of vorticity at the point $(0.95, 0.95)$, chosen based on information in Fig. 1. Overall, the dynamics is characterized in Fig. 2, by an onset showing irregular transient

behavior (in Range-1a), followed by coherent temporal decay of the time series in Range-1b. Range-2 represents quiescent state. In this figure, Range-3a is defined as the region where the flow experiences an instability, which in the literature is often analyzed by linearized temporal theory. Secondary instability marked as Range-3b in the time series for $Re = 9300$ has an onset from $Re = 9100$ onwards. Such secondary instability of limit cycle can also be regarded as nonlinear instability and is reported for the flow inside LDC. In Fig. 2, Range-4 demarcates the stable limit cycle for $Re = 8800$ case. It is noted that the time at which the final limit cycle is reached varies greatly with Re.

Present DNS-based approach to study Hopf bifurcations is distinct from that in the literature, where normal mode instability analysis is attempted for steady state solutions. Here, we show multiple Hopf bifurcations in the range $8000 \leq Re \leq 12000$, for the unexcited impulsively started cases. Also, we do not project solution from one Re to another, as this is shown to produce erroneous flows, as shown in subsection 6.2 (Fig. 11) especially near Hopf bifurcations. In [3], the authors have reported a possible second bifurcation for a supposed range of [9687, 9765).

The limit cycle amplitude variation with respect to Re has been used to characterize Hopf bifurcations. In Fig. 6, it is shown that A_e^2 is proportional to Re on different segments of Re for the unexcited cases, which are clearly separated from one to the next bifurcation. For the (257×257)-grid, the Hopf bifurcations for unexcited case are located at $Re_{cr1} = 8660$ followed by $Re_{cr2} = 9400$, $Re_{cr3} \in [10500, 10700]$ and $Re_{cr4} = 11700$.

Here $Re_{cr1} \approx 8660$ is noted for the case of no excitation, and such a high value is due to higher accuracy of the method discussed in section 6.1, with low aliasing error responsible in triggering unsteadiness. This value has been lowered by the application of explicit excitation, in the form of a pulsating vortex placed near the top left corner. Following this procedure, it has been shown that Re_{cr1} can be lowered to as small a value in between 8020 and 8025, shown in Fig. 12 and described in section 6.3.

Investigated LDC flow is characterized by multiple time scales at any Re, which are weak function of Re in selective intervals, punctuated by multiple bifurcations, as shown in Table 2. Further investigation of bifurcations are made with FFT of time series results shown in Fig. 7. The lower post-critical Re cases show distinct harmonics, while the case for $Re = 9400$ has unique pattern of triplet of harmonics, as also noted in Table 2. The very high Re cases are characterized by broadband spectrum, with many peaks and having

two incommensurate dominant frequencies as noted in the bottom frame of Fig. 7. Phase portraits are plotted over a time interval of 100 units, further showing vorticity and its time rate, which show trajectories for very stable limit cycles for low Re cases with very narrow basin of attractors, which are unlike the last two segments, where trajectories belong to larger dispersed bands with wider basin of attractors. This irregularity is observed in vorticity contours for higher Re, where one notices the basin as a continuous sheet resembling a Möbius strip.

In conclusion, we explain the universality of the primary Hopf bifurcation Reynolds number, Re_{cr1}, by showing the effects of pulsating a vortex at a fixed frequency near the top left corner of the LDC. Presented results in Figs. 12 to 14 show the universal value of Re_{cr1} to be within the range of 8020 and 8025. The present investigation achieves two primary goals: First, it reconciles that Re_{cr1} obtained by different numerical approaches can be shown in identical range, provided the equilibrium flow obtained is of good quality, untainted by excessive diffusion. The present high accuracy computation, on the other hand, require explicit excitation to obtain Re_{cr1} towards the *universal* value of the same. This is shown here for the first time reconciling high accuracy approach for DNS with results based on global stability analysis.

[1] Sengupta T. K., Ganeriwal G. and De S., Analysis of central and upwind compact schemes, *J. Comput. Phys.,* **192***, 677-694* (2003).

[2] Auteri F., Quartapelle L. and Vigevano L., Accurate ω-ψ spectra; solution of the singular driven cavity problem, *J. Comput. Phys.,* **180***, 597-615* (2002).

[3] Auteri F., Parolini N. and Quartapelle L., Numerical investigation on the stability of singular driven cavity flow, *J. Comput. Phys.,* **183***, 1-25* (2002).

[4] Beckers M. and van Heijst G. J. F., The observation of a triangular vortex in a rotating fluid, *Fluid Dyn. Res.,* **22***, 265-279* (1998).

[5] Bender C. M. and Orszag S. A., *Advanced Mathematical Methods for Scientists and Engineers I: Asymptotic Methods and Perturbation Theory*, Springer, USA (1999).

[6] Boppana V. B. L. and Gajjar J. S. B., Global flow instability in a lid-driven cavity, *Int. J. Num. Meth. Fluids,* **62***, 827-853* (2009).

[7] Botella O. and Peyret R., Benchmark spectral results on the lid-driven cavity flow, *Comput. Fluids,* **24***, 421-433* (1998).

[8] Bruneau C. H. and Saad M., The 2D lid-driven cavity problem revisited, *Comput. Fluids,* **35***(3), 326-348* (2006).

[9] Burgraff O. R. Analytical and numerical study of the structure of steady separated flows, *J. Fluid Mech.,* **24***, 113-151* (1966).

[10] Carnevale G. F. and Kloosterziel R. C., Emergence and evolution of triangular vortices, *J. Fluid Mech.,* **259***, 305-331* (1994).

[11] Cazemier W., Verstappen R. W. C. P. and Veldman A. E. P., Proper orthogonal decomposition and low-dimensional models for driven cavity flows, *Physics Fluids,* **10***(7) 1685-1699* (1998).

[12] Drazin P. G. and Reid W. H., *Hydrodynamic Stability*, Cambridge Univ. Press, UK (1981).

[13] Eckhaus W., *Studies in Nonlinear Stability Theory*, Springer: Berlin (1965).

[14] Erturk E., Corke T. C., Gökcöl C., Numerical solutions of 2-D steady incompressible driven cavity flow at high Reynolds numbers, *Int. J. Num. Meth. Fluids,* **48***(7), 747-774* (2005).

[15] U. Fey, M. König and H. Eckelmann, A new Strouhal-Reynolds-number relationship for the circular cylinder in the range 47<Re $< 2\times 10^5$, *Phys. Fluids,* **10***, 1547* (1998).

[16] Fortin A., Jardak M., Gervais J. J. and Pierre R., Localization of Hopf bifurcations in fluid flow problems, *Int. J. Num. Meth. Fluids,* **24***(11), 1185-1210* (1997).

[17] Ghia U., Ghia K. N. and Shin C. T., High-Re solutions for incompressible flow using the NavierStokes equations and a multigrid method, *J. Comput. Phys.,* **48***, 387-411* (1982).

[18] Goodrich J. W., Gustafson K. and Halasi K., Hopf bifuraction in the driven cavity, *J. Comput. Phys.,* **90***, 219-261* (1990).

[19] Gustafson K. and Halasi K., Vortex dynamics of cavity flows, *J. Comput. Phys.,* **64***, 279-319* (1986).

[20] Hancock C., Lewis E. and Moffatt H. K., Effect of inertia in forced corner flows, *J. Fluid Mech.,* **112***, 315-327* (1986).

[21] Schmid P. J. and Henningson D. S., *Stability and Transition in Shear Flows*, Springer Verlag: New York (2001).

[22] Jansson T. R. N., Haspang M. P., Jensen K. H., Hersen P. and Bohr, T., Polygons on a rotating fluid surface, *Phys. Rev. Lett.,* **96***, 174502* (2006).

[23] Sengupta T. K., Singh N. and Suman V. K., Dynamical system approach to instability of flow past a circular cylinder, *J. Fluid Mech.,* **656***, 82-115* (2010).

[24] Landau L. D. and Lifshitz E. M., *Fluid Mechanics*, Pergamon Press, UK (1959).

[25] E. Leriche, Direct Numerical Simulation in a Lid-Driven Cubical Cavity at High Reynolds Number by a Chebyshev Spectral Method, *J. Sci. Comput.* **27**, *335-345* (2006).

[26] Sengupta T. K., Lakshmanan V. and Vijay V. V. S. N., A new combined stable and dispersion relation preserving compact scheme for non-periodic problems, *J. Comput. Phys.,* **228***, 3048-3071* (2009).

[27] Sengupta T. K., Vijay V. V. S. N. and Bhaumik S, Further improvement and analysis of CCD scheme: Dissipation discretization and dealiasing properties, *J. Comput. Phys.,* **228***, 6150-6168* (2009).

[28] Osada T. and Iwatsu, R., Numerical simulation of unsteady driven cavity flow, *J. The Phys. Soc. Japan.* **80***, 094401* (2011).

[29] Peng Y.-F., Shiau Y.-H. and Hwang R. R.. Transition in a 2-D lid-driven cavity flow, *Comput. Fluids,* **32***, 337-352* (2003).

[30] Poliashenko M., Aidun C. K., A direct method for computation of simple bifurcations. *J. Comput. Phys.,* **121***(2), 246-260* (1995).

[31] Sengupta T. K., Haider S. I., Parvathi M. K. and Pallavi G., Enstrophy-based proper orthogonal decomposition for reduced-order modeling of flow past a cylinder, *Phys. Rev. E,* **91***, 043303* (2015).

[32] Sahin M. and Owens R. G., A novel fully-implicit finite volume method applied to the lid-driven cavity problem. Part II. Linear stability analysis, *Int. J. Num. Meth. Fluids,* **42***, 79-88* (2003).

[33] Schreiber R. and Keller H. B., Driven cavity flows by efficient numerical techniques, *J. Comput. Phys.,* **49***, 310-333* (1983).

[34] Shen J., Hopf bifurcation of the unsteady regularized driven cavity flow , *J. Comput. Phys.,* **95***, 228* (1991).

[35] Sengupta T. K., Instabilities of Flows and Transition to Turbulence, CRC Press, USA (2012).

[36] Sengupta T. K., High Accuracy Computing Methods: Fluid Flows and Wave Phenomena, Cambridge Univ. Press, USA (2013).

[37] Sengupta T. K. and Nair M. T., Upwind schemes and large eddy simulation, *Int. J. Num. Meth. Fluids,* **31***(5), 879-889* (1999).

[38] Sengupta T. K., Singh N. and Vijay V. V. S. N., Universal instability modes in internal and external flows, *Comput. Fluids,* **40***, 221-235* (2011).

[39] Seydel R., *Practical Bifurcation and Stability Analysis from Equilibrium to Chaos*, Springer: Berlin (1994).

[40] Stuart J. T., On the nonlinear mechanics of wave disturbances in stable and unstable parallel flows. Part 1. The basic behaviour in plane Poiseuille flow, *J. Fluid Mech.,* **9***, 353-370* (1960).

[41] Suman, V.K., Sengupta, T. K., Prasad, C. J. D., Mohan, K. S. and Sanwalia, D., Spectral analysis of finite difference schemes for convection diffusion equation, *Computers and Fluids, 150, 95-114* (2017).

[42] Van der Vorst H. A., Bi-CGSTAB: a fast and smoothly converging variant of Bi-CG for the solution of non-symmetric linear systems, *SIAM J. Sci. Stat. Comput.,* **12***, 631- 644* (1992).

[43] Yu C. H., Bhumkar Y. G. and Sheu Tony W. H., Dispersion relation preserving combined compact difference schemes for flow problems, *J. Sci. Comput.* **62***, 482-516* (2015).

[44] Sengupta T. K., Dipankar, A. and Sagaut, P., Error dynamics: Beyond von Neumann analysis, *J. Comput. Phys.* **226(2), 1211-1218** (2007).

[45] C. David, P. Sagaut and T.K. Sengupta, A linear dispersive mechanism for numerical error growth: Spurious caustics, *Euro. J. Mechanics B/Fluids* **28***(1), 146-151* (2009)

[46] Girault, G., Guevel, Y., Cadou, J. M., An algortihm for the computation of multiple Hopf bifurcation points based on Pad/'e approximants, *Int. J. Num. Methods Fluids* **68***, 1189-1206* (2012)